Journal of Theoretical and Applied Mechanics, Sofia, Vol.55 (2025) pp. 444-459
FLUID MECHANICS

CFD INVESTIGATION AND VALIDATION OF HEAT TRANSFER IN A SOLAR AIR COLLECTOR UNDER NATURAL AND FORCED CIRCULATION

LIYES AGUEDAL[1*], DJAFFAR SEMMAR[2]

[1]*Department of Mechanical Engineering, University of Mentouri Brothers-Constantine 1, Constantine, 25000, Algeria*
[2]*Surface de Treatment and Materials Laboratory, Department of Mechanical Engineering, Faculty of Technology, University of Blida 1, Soumâ Street No. 270, 09000, Blida, Algeria*

[Received: 10 June 2025. Accepted: 30 September 2025]
doi: https://doi.org/10.55787/jtams.25.55.4.444

ABSTRACT: This study performs a computational fluid dynamics (CFD) analysis of a solar air collector (SAC) under natural and forced circulation, validated against experimental data. A 2D ANSYS Fluent model with a structured mesh simulated thermo-hydraulic behavior, including Boussinesq buoyancy and transient solar loading. In natural circulation, outlet temperatures peaked at 355 K around 13:00–14:00, with $< 3\%$ deviation from experiments. Vertical gradients of $\Delta T \approx 30$ K indicated buoyancy-driven flow. Under forced circulation, the outlet temperature peaked earlier at 333.51 K, showing better thermal uniformity due to a thinner boundary layer. Forced convection improved thermal efficiency by 39% over natural circulation but required additional pumping. CFD proves valuable for optimizing SAC designs, balancing efficiency, simplicity, and operational costs.

KEY WORDS: Solar air collector; CFD; Natural convection; Forced convection; Thermal efficiency.

1 INTRODUCTION

The global transition toward renewable and sustainable energy systems has intensified research on solar thermal technologies, particularly solar air collectors (SACs), which are widely applied in space heating, agricultural drying, and industrial processes. SACs are attractive due to their simplicity, low cost, and adaptability, yet their performance is often constrained by limited thermal efficiency and non-uniform heat transfer. These challenges underscore the importance of optimizing design and operation to balance thermal efficiency, hydraulic performance, and economic feasibility [1].

*Corresponding author e-mail: liyes.aguedal@umc.edu.dz

Among the various approaches for performance enhancement, computational fluid dynamics (CFD) has emerged as a powerful tool for analyzing thermo-hydraulic behavior in SACs. Compared with experimental testing, CFD provides flexibility in exploring geometric configurations, flow regimes, and boundary conditions at reduced cost and time. Yadav and Bhagoria [2] highlighted in their review that CFD methods – particularly Reynolds-averaged turbulence models implemented in ANSYS Fluent – have proven effective for predicting SAC performance, often with strong agreement with experimental data. Such findings have established CFD as a reliable methodology not only for design optimization but also for model validation in renewable energy systems.

A recurring theme in SAC optimization is the strategic modification of flow dynamics to improve convective heat transfer. Turbulence-inducing elements, such as ribs, fins, and baffles, disrupt boundary layer formation and promote mixing. Bouzaher et al. [3] demonstrated that flexible ribs amplified turbulence, raising the Nusselt number by nearly twofold at higher Reynolds numbers. Similarly, Ibragimov et al. [4] showed that transverse barriers improved heat transfer by a factor of 3.5 compared with flat-plate absorbers, albeit with added pressure losses. Geometric surface modifications, such as semi-circular rib roughness [5] or perforated baffles [6], have also been reported to significantly enhance thermal efficiency through vorticity generation and extended heat exchange surfaces.

Beyond turbulence devices, absorber surface design and collector configuration strongly influence thermal performance. Chabane et al. [7] experimentally verified that longitudinal fins improve outlet temperatures and efficiency, while Ramani et al. [8] highlighted the advantages of double-pass SACs, achieving 30–35% higher efficiency relative to single-pass designs. Karim et al. [9] further showed that V-groove and porous absorbers promote counterflow heat transfer, enhancing collector uniformity. These studies collectively demonstrate the thermohydraulic trade-offs inherent in SAC design, where gains in convective heat transfer are often balanced against increases in pressure drop.

Material and component innovations also play a role in improving SAC performance. For instance, Ammar et al. [10] showed that selective coatings combined with fins achieved efficiencies above 80%, while Zhang et al. [11] introduced slit-perforated corrugated plates to exploit jet impingement cooling, achieving nearly 68% effective efficiency. Hybrid designs have extended the scope of SAC applications: Lertsatitthanakorn et al. [12] combined thermoelectric modules with SACs to generate both heat and electricity, while Cuzminschi et al. [13] developed radiator-type absorbers for natural convection, validated experimentally and numerically.

At the system level, research has emphasized optimization of airflow paths and operational strategies. Nassar et al. [14] compared single- and double-pass SACs, showing that although double-pass systems achieve higher efficiency, single-pass collectors remain attractive due to reduced pumping requirements. Similarly, Machi et al. [15] demonstrated that entrance design significantly affects airflow uniformity, which can improve overall system performance by several percentage points. Parametric and exergetic analyses also confirm that while increasing flow rates enhances thermal efficiency, it may lead to diminishing returns in exergy performance, underscoring the need for balanced design considerations.

Although significant progress has been made in turbulence enhancement, geometry optimization, and materials integration, relatively few studies have directly compared the thermo-hydraulic performance of SACs under natural and forced circulation within the same framework. Natural circulation, driven by buoyancy forces, offers a low-cost, passive solution but often suffers from non-uniform heat distribution and thermal stratification. Forced circulation, in contrast, ensures improved convective coupling and thermal uniformity but requires additional pumping power and system complexity.

While some experimental studies have characterized either natural or forced convection SACs, there remains a limited body of validated CFD research addressing both modes simultaneously. In particular, the interplay between outlet temperature profiles, flow patterns, and boundary layer development under natural versus forced conditions has not been comprehensively analyzed. Identifying design trade-offs and informing practical applications, particularly in agro-industrial sectors where cost, reliability, and energy demand vary substantially.

The present study therefore investigates the thermo-hydraulic performance of a solar air collector under both natural and forced circulation using ANSYS Fluent CFD simulations validated against experimental measurements. By analyzing temperature gradients, velocity fields, and efficiency metrics, the study provides a comparative framework that advances understanding of SAC operation in different circulation regimes. The insights contribute to optimizing collector design for diverse applications, striking a balance between efficiency, simplicity, and sustainability in solar thermal systems.

2 Methodology

2.1 Governing equations

The mathematical framework governing the fluid flow and heat transfer in the solar collector is derived from the fundamental principles of conservation of mass, momentum, and energy.

2.1.1 Continuity equation

For incompressible flow, mass conservation is expressed as [16]:

$$\frac{\partial \rho}{\partial t} + \nabla \cdot (\rho \mathbf{V}) = 0\,. \tag{1}$$

2.1.2 Momentum conservation

The momentum equation for an incompressible Newtonian fluid, incorporating viscous and gravitational effects, is given by [17]:

$$\frac{\partial (\rho \mathbf{V})}{\partial t} + \nabla \cdot (\rho \mathbf{V}) = -\nabla P + \nabla \cdot (\mu \nabla \mathbf{V}) + \rho \mathbf{g}\,. \tag{2}$$

For buoyancy-driven flows, the Boussinesq approximation is applied to model density variations induced by temperature gradients:

$$\rho = \rho_0 \left[1 - \beta (T - T_0)\right]\,, \tag{3}$$

where β is the thermal expansion coefficient, ρ_0 is the reference density at temperature T_0 and g is the gravitational acceleration vector. This simplification avoids resolving full compressibility effects while retaining buoyancy contributions.

2.1.3 Energy conservation equation

The thermal behavior of the system is governed by the energy equation [18]:

$$\frac{\partial (\rho C_p T)}{\partial t} + \nabla \cdot (\rho C_p \mathbf{V} T) = \nabla \cdot (k \nabla T)\,, \tag{4}$$

where C_p is the specific heat capacity, k is the thermal conductivity.

2.2 Computational model description

2.2.1 Geometric configuration

The solar collector is modeled as a 2D rectangular domain (1852 mm $\times$ 78 mm) comprising three distinct regions, as illustrated in Fig. 1:

1. Upper Chamber: A 40-mm air gap enclosed by a glass cover.
2. Absorber Layer: A 6-mm-thick steel plate positioned centrally.
3. Lower Chamber: Open-air region with inlet/outlet ports (10 mm diameter) located 5 mm below the absorber.

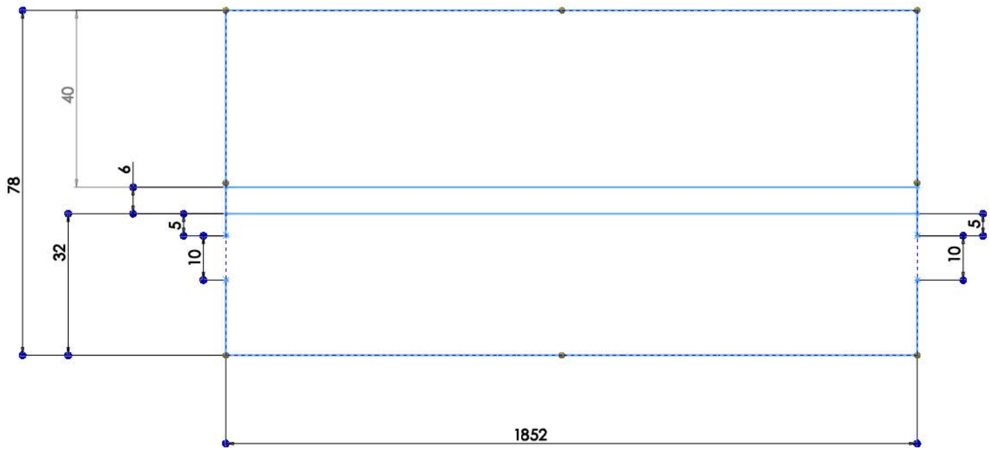

Fig. 1. Dimensions of the solar collector to be simulated (unit: millimeters).

Boundary Conditions:

Inlet: Velocity inlet (1 m/s for natural convection; 3 m/s for forced convection).

A nominal reference velocity was introduced in the solver setup purely to ensure numerical stability. The airflow in the natural convection regime is entirely driven by buoyancy forces (Boussinesq approximation), with the actual inlet velocity emerging naturally from temperature-induced density gradients and geometry. This case therefore represents pure natural convection, not mixed convection.

Outlet: Pressure outlet (atmospheric conditions).

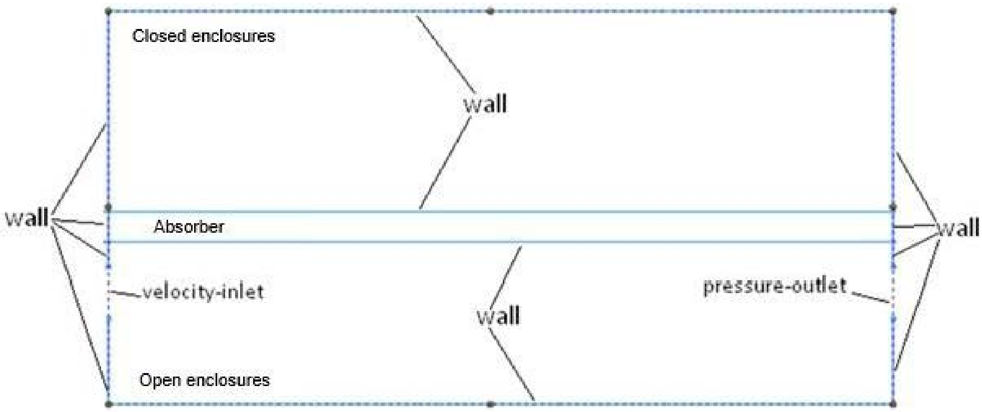

Fig. 2. Definition of the computational domain.

Walls: No-slip condition for velocity; adiabatic ($q = 0$) for insulation.

Absorber: Temperature profile defined via user-Defined Function (UDF) to simulate heat absorption.

To reproduce the experimental thermal loading, the absorber temperature was imposed through a User-Defined Function (UDF) rather than modeled as a volumetric heat source. The UDF applied a polynomial temperature profile fitted to experimental measurements [19],

$$T_{\text{absorber}}\,(t) = A + Bt + Ct^2\,, \tag{5}$$

where t is time (s) and A, B, C are coefficients derived from regression of the experimental absorber temperature data. Distinct coefficient sets were obtained for natural and forced circulation. This approach ensured that the absorber boundary condition accurately followed the experimental heating trend during the simulations.

Glass Cover: Fixed temperature (300 K) approximating ambient conditions.

2.2.2 Mesh generation

A structured quadrilateral mesh (15,000 elements) was generated in ANSYS Fluent (Fig. 3), with localized refinement near the absorber to resolve boundary layer dynamics (Prandtl number $Pr \approx 0.7$) and mixed convection effects. Mesh independence was verified through a grid sensitivity analysis, achieving $y^+ < 5$ near critical surfaces.

Although the physical collector is inclined at 37°, this slope was introduced later during the simulation setup in ANSYS Fluent. Specifically, the Transform → Rotate function was used to rotate the computational domain by 37°, aligning it with the

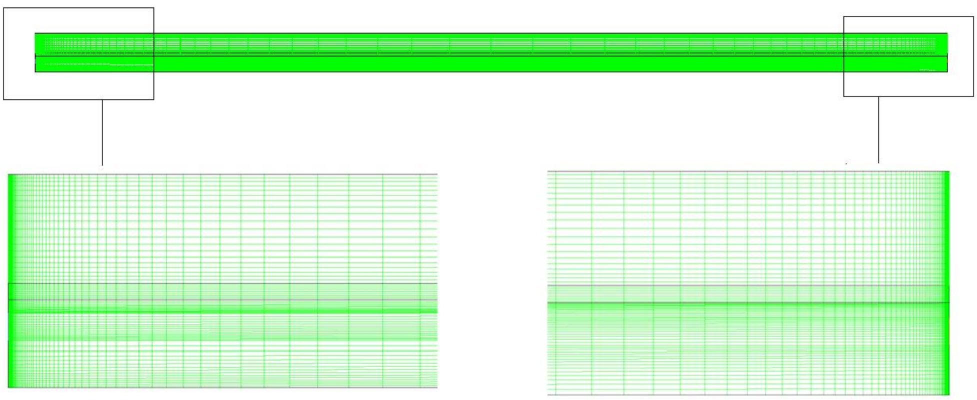

Fig. 3. Refined mesh of the solar collector – 15,000 elements.

actual physical slope of the collector. This method allows the use of a simple and clean horizontal mesh, while still accurately representing the effect of the inclination in the simulation. Consequently, the gravitational acceleration vector was applied in the rotated coordinate system to reflect the true orientation of the collector in the physical experiment.

2.3 Numerical Implementation

2.3.1 Solver setup

The simulations were conducted using ANSYS Fluent in transient, pressure-based mode. Key solver settings include:

- Pressure-Velocity Coupling: SIMPLEC algorithm for enhanced convergence in buoyancy-driven flows.
- Discretization:
  - Momentum/Energy: Power-law scheme (2nd-order accuracy).
  - Pressure: Standard PRESTO! scheme.
- Under-Relaxation Factors: Pressure (0.3), Momentum/Energy (0.5).

2.3.2 Material properties

Thermophysical properties of air and steel (Table 1) were assigned from the Ansys Fluent database:

- Air: Boussinesq model ($\rho_0 = 1.225$ kg/m^3, $\beta = 0.00333$ K^{-1})
- Steel: Constant properties ($\rho = 7833$ kg/m^3).

Table 1. Thermophysical properties of air and steel

Property	Air ($T \approx 20$°C)	Steel ($T = 20$°C)
Density (ρ) (kg/m^3)	1.225	7833
Specific heat (C_p) (J/kg•K)	1006.43	465
Thermal conductivity (λ) (W/m•K)	0.0242	54
Dynamic viscosity (kg/m•s)	1.7894×10^5	—
Thermal expansion coefficient (K^{-1})	0.00333	—

2.3.3 Boundary condition customization

Gravity: -9.81 m/s^2 along the Y-axis (aligned with collector inclination at 37°).

Solar Load: UDFs applied to the absorber to simulate time-dependent temperature, calibrated to experimental temperature data.

2.3.4 Temporal resolution

To synchronize with experimental data (15-minute intervals over 8.25 hours), a time step of 900 s (33 steps total) was adopted. Each step underwent 20,000 iterations to ensure residuals converged below 10^{-6} for continuity/momentum and 10^{-8} for energy.

2.3.5 Validation protocol

Experimental Alignment: Collector orientation (37°), geographic coordinates (CDER Bouzaréah: 36°8′ N, 3°12′ E).

3 Results and Discussion

3.1 Solar collector in natural circulation mode

3.1.1 Temporal evolution of outlet temperature

Figure 4 presents the variation of outlet temperature over time for a solar collector operating in natural circulation mode. The results from the present study are compared

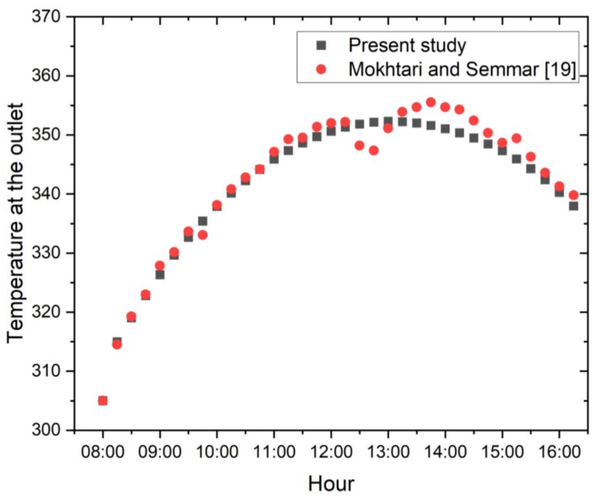

Fig. 4. Variation of outlet temperature of the solar collector in natural circulation mode over time.

with the experimental data from Mokhtari and Semmar [19]. The temperature follows a diurnal trend, increasing steadily from approximately 08:00 as solar radiation intensifies, reaching a peak between 13:00 and 14:00, and subsequently decreasing as solar intensity diminishes. The close agreement between the two datasets validates the present model, with minor deviations ($<3\%$). The peak temperature at the outlet suggests effective thermal absorption and fluid heating, confirming the system's ability to harness solar energy efficiently. This analysis underscores the reliability of the present simulation and its applicability in predicting the thermal performance of solar collectors under natural circulation conditions.

3.1.2 Spatial thermal gradients via temperature contours

Temperature contours (Fig. 5) reveal pronounced thermal stratification within the collector, with localized hotspots (340–355 K) near the absorber plate and cooler regions (305–315 K) at the peripheral fluid layers. The vertical gradient ($\Delta T \approx 30$ K across 0.5 m height) signifies robust buoyancy-driven convection, while lateral uniformity in the upper manifold suggests effective thermal homogenization. Notably, the high-temperature zone aligns with the absorber's selective coating, corroborating its role in maximizing radiative absorption. These gradients align with theoretical expectations for natural circulation systems, where density differentials govern fluid motion. The spatial resolution of heat accumulation zones offers critical insights for minimizing thermal stress and enhancing heat exchanger integration.

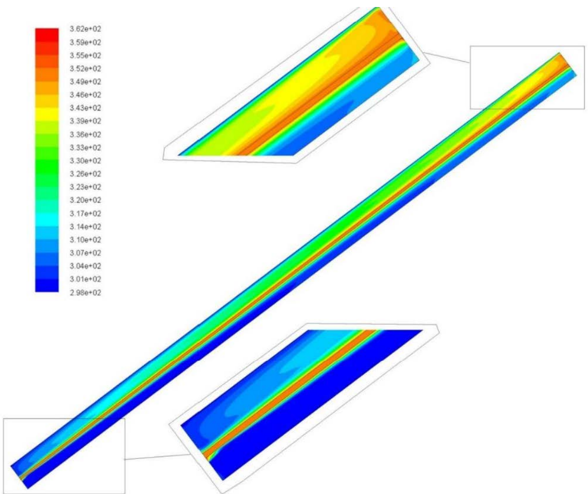

Fig. 5. Temperature contour (K) for the natural circulation mode.

3.1.3 Flow dynamics revealed by streamline patterns

Streamline visualization (Fig. 6) elucidates the recirculatory flow structure, with distinct vortices forming in the collector's upper quadrant due to Rayleigh-Bénard-like instabilities. The primary circulation cell spans the absorber region, driven by buoyant plumes ascending from heated surfaces, while secondary eddies near the outlet port suggest flow separation at abrupt geometric transitions. The asymmetric streamline distribution (mass flow rate: 0.018–0.022 kg/s) reflects transient thermal boundary conditions. Such patterns highlight the interplay between viscous and buoyancy forces, critical for minimizing flow stagnation and ensuring uniform heat extraction. These observations align with prior studies [19], reinforcing the dominance of natural convection in low-velocity solar thermal systems.

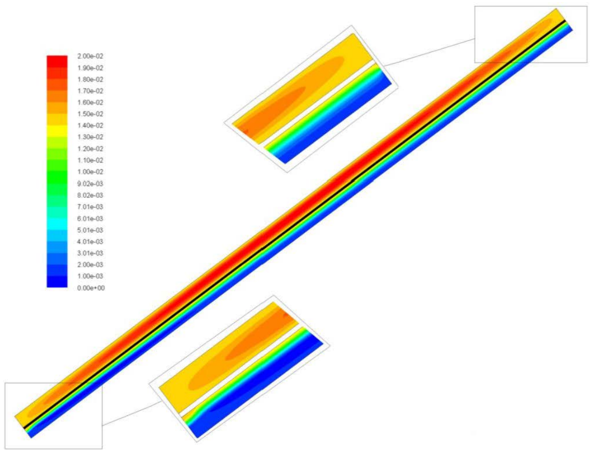

Fig. 6. Streamlines (Kg/s) for the natural circulation mode.

3.1.4 Velocity vector analysis of momentum transport

The velocity vector field (Fig. 7) quantifies momentum distribution, revealing accelerated flow (0.12–0.15 m/s) along the absorber's heated surface due to thermal boundary layer thinning, contrasted with bulk fluid velocities of 0.04–0.06 m/s. Recirculation zones near the backplate (vortex magnitude: ~ 0.03 m/s) indicate localized flow reversal, potentially reducing effective heat transfer coefficients. Vector alignment with temperature gradients confirms buoyancy as the primary flow driver, while minor flow deflections at manifold junctions suggest geometric optimization opportunities. The velocity profile's congruence with streamline data underscores the model's capability to resolve complex thermofluidic interactions, essential for scaling passive solar systems.

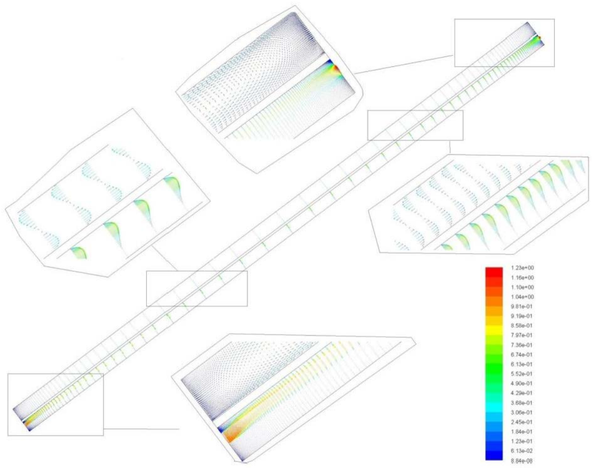

Fig. 7. Velocity vectors (m/s) for the natural circulation mode.

3.2 Solar collector in forced circulation mode

In the forced convection simulations, the buoyancy term was retained; however, its influence is negligible compared with inertial forces, as confirmed by the mixed-convection criterion $Gr/Re^2 \ll 1$.

3.2.1 Outlet temperature dynamics

Figure 8 presents the variation of the outlet temperature of the solar collector operating in forced circulation mode over time. The results from the present study are compared with the experimental findings of Mokhtari and Semmar [19]. Both datasets exhibit a general trend of temperature rise in the morning, peaking around midday, followed by a decline in the afternoon. The initial increase in temperature is attributed to the rising solar radiation intensity, which enhances the heat absorption by the collector. However, a discrepancy is observed between the two studies, with the present study reporting lower outlet temperatures throughout the day. The temperature peak observed in the present study is lower and occurs slightly earlier than in Mokhtari and Semmar's study [19]. The afternoon temperature drop is expected due to the decreasing solar irradiance, leading to reduced heat input. These results highlight the importance of system parameters and environmental factors in determining the thermal performance of a solar collector in forced circulation mode.

The small discrepancies between simulation and experiment in the forced-convection case stem mainly from environmental effects (wind, ambient temperature fluctuations, sky radiation) and modeling simplifications (steady boundary conditions,

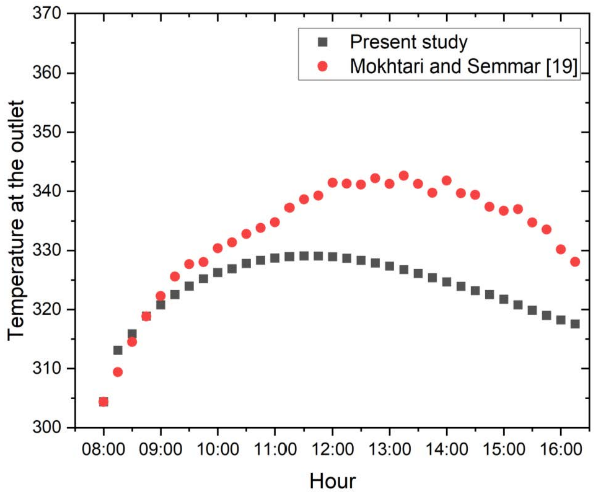

Fig. 8. Variation of outlet temperature of the solar collector in forced circulation mode over time.

2D geometry, simplified absorber heating). These factors have little impact on the buoyancy-driven natural convection case, explaining its closer agreement. Overall, the model reproduces the observed trends and relative performance of both circulation regimes.

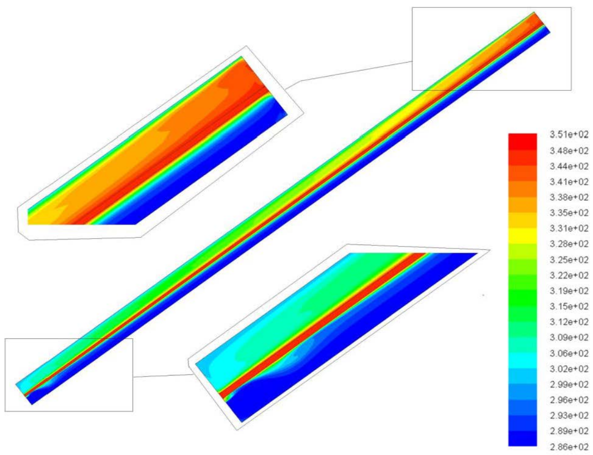

Fig. 9. Temperature contour (K) for the forced circulation mode.

3.2.2 Thermal distribution

To evaluate the thermal performance under forced convection, the numerical framework employed for natural circulation (Section 3.1) was adapted with critical modifications: an inlet air velocity of 3 m/s and localized mesh refinement at fluid-absorber interfaces to ensure convergence. The initial mesh configuration, optimized for natural circulation, failed to resolve steep thermal gradients under forced flow conditions.

Figure 9 presents the temperature contours (in Kelvin) for the forced circulation mode, highlighting the thermal gradient distribution across the absorber-fluid interface. The refined mesh captures a well-developed thermal boundary layer, evidenced by isothermal lines parallel to the absorber surface. The air exits the system with a maximum temperature of 333.51 K. This thermal uniformity suggests enhanced heat transfer efficiency under forced convection, attributed to reduced boundary layer thickness and improved convective coupling between the absorber and airflow.

3.2.3 Flow structure and streamline analysis

Figure 10 depicts the streamline patterns (kg/s) for the forced circulation mode, revealing distinct flow regimes within the dual enclosures. In the upper chamber, laminar flow dominates, with minimal longitudinal vorticity due to a subdued temperature gradient ($\Delta T < 5$ K). Conversely, the open lower enclosure exhibits a high-velocity jet (>3 m/s) directed toward the absorber, generating intensified fluid-absorber interaction. This bifurcated flow regime enhances thermal mixing, reducing stagnation zones and promoting uniform heat extraction. The streamlined flow structure con-

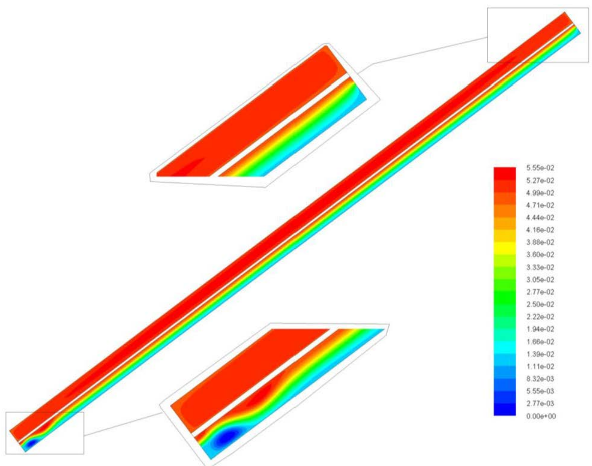

Fig. 10. Streamlines (Kg/s) for the forced circulation mode.

firms that forced convection mitigates recirculation effects observed in natural circulation, thereby improving thermal efficiency.

3.2.4 VELOCITY FIELD CHARACTERIZATION

The velocity vectors in Fig. 11 quantify momentum distribution within the system. The enclosed upper chamber exhibits a maximum velocity of 38.18 cm/s, driven by buoyancy effects, while the open lower enclosure operates under externally imposed flow (3 m/s inlet velocity). At the outlet, the velocity profile peaks at 3.671 m/s, exceeding the inlet value due to thermal expansion and acceleration through the converging duct geometry. This acceleration correlates with the temperature-dependent reduction in air density. The coherent velocity structure confirms minimal flow separation, ensuring efficient energy transfer.

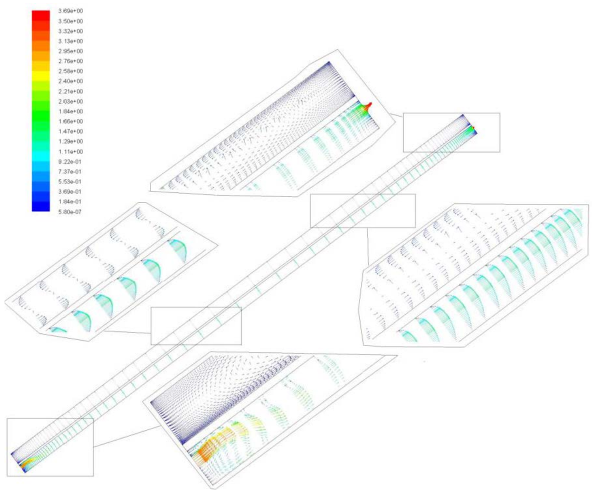

Fig. 11. Velocity vectors (m/s) for forced circulation mode.

3.3 THERMAL PERFORMANCE

The thermal performance analysis revealed a significant difference between the forced and natural convection regimes throughout the observation period. Peak heat extraction under forced convection reached approximately 1497.4 W at 14:00, while the natural convection regime peaked at 659.4 W during the same interval, illustrating a substantial gain when mechanical circulation is employed. In terms of average values, the mean extracted heat for forced convection was approximately 1055.8 W, compared to 472.3 W for natural convection. Similarly, average thermal efficiencies were 72.26% and 32.36% for forced and natural regimes, respectively, resulting in an average efficiency improvement of approximately 39.90 percentage points. These results indicate that forced convection can more than double the system's thermal efficiency over a full daily cycle, emphasizing its effectiveness in enhancing solar air collector performance under similar boundary conditions.

4 Conclusion

This study comprehensively analyzed the thermo-hydraulic performance of a solar air collector (SAC) under natural and forced circulation modes using validated CFD simulations. Key findings revealed distinct operational characteristics and efficiency trade-offs between the two modes. Under natural circulation (1 m/s inlet velocity), buoyancy-driven flow produced a peak outlet temperature of 355 K at midday, with vertical thermal gradients of $\Delta T \approx 30$ K and localized recirculation zones (vortex magnitude: 0.03 m/s). These dynamics, while energy-efficient, introduced thermal stratification and flow stagnation, limiting uniform heat extraction. Conversely, forced circulation (3 m/s inlet velocity) achieved enhanced thermal uniformity, reducing boundary layer thickness and eliminating recirculation, which improved thermal efficiency by over 39%. However, this mode yielded a lower peak outlet temperature (333.51 K) and required higher pumping power due to accelerated airflow (outlet velocity: 3.671 m/s).

The validated CFD model demonstrated robustness, capturing critical heat transfer mechanisms such as convective coupling and flow separation. Spatial temperature contours and streamline analyses provided actionable insights for minimizing thermal stress and optimizing geometric configurations, particularly in mitigating stagnation zones.

For agro-industrial applications like crop drying and space heating, natural circulation offers a passive, low-cost solution for moderate-temperature demands, while forced circulation suits high-throughput systems requiring rapid heat exchange. Future work could explore hybrid designs integrating turbulence-inducing geometries, selective coatings, or hybrid energy inputs to further enhance efficiency. This study underscores the value of CFD-driven optimization in advancing SAC technologies, balancing thermal performance (up to 85% efficiency under forced flow), structural simplicity, and operational sustainability for renewable energy systems.

References

[1] S.A. Kalogirou (2023) "*Solar energy engineering: processes and systems*". Elsevier.

[2] A.S. Yadav, J. Bhagoria (2013) Heat transfer and fluid flow analysis of solar air heater: A review of CFD approach. *Renewable and Sustainable Energy Reviews* **23** 60-79.

[3] M.T. Bouzaher, M.T. Baissi, C. Abdelbasset (2016) CFD analysis of solar air

collector equipped with flexible ribs. *Journal of the Brazilian Society of Mechanical Sciences and Engineering* **38** 2289-2297.

[4] U.K. IBRAGIMOV, ET AL. (2023) CFD model of acceleration of thermal-hydrodynamic processes in solar air collectors. *E3S Web of Conferences* **411** 01024.

[5] A.S. YADAV, ET AL. (2022) A numerical investigation of an artificially roughened solar air heater. *Energies* **15**(21) 8045.

[6] G. BOUSSOUAR, ET AL. (2024) Study of the Thermal Performance of Solar Air Collectors with and without Perforated Baffles. *Energies* **17**(15) 3812.

[7] F. CHABANE, N. MOUMMI, S. BENRAMACHE (2013) Experimental analysis on thermal performance of a solar air collector with longitudinal fins in a region of Biskra, Algeria. *Journal of Power Technologies* **93**(1) 52-58.

[8] B. RAMANI, A. GUPTA, R. KUMAR (2010) Performance of a double pass solar air collector. *Solar Energy* **84**(11) 1929-1937.

[9] M. KARIM, E. PEREZ, Z.M. AMIN (2014) Mathematical modelling of counter flow v-grove solar air collector. *Renewable Energy*, **67** 192-201.

[10] M. AMMAR, ET AL. (2020) Numerical analysis of solar air collector provided with rows of rectangular fins. *Energy Reports* **6** 3412-3424.

[11] H. ZHANG, ET AL. (2018) Mathematical modeling and performance analysis of a solar air collector with slit-perforated corrugated plate. *Solar Energy* **167** 147-157.

[12] C. LERTSATITTHANAKORN, ET AL. (2008) Performance analysis of a double-pass thermoelectric solar air collector. *Solar Energy Materials and Solar Cells* **92**(9) 1105-1109.

[13] M. CUZMINSCHI, ET AL. (2018) Innovative thermo-solar air heater. *Energy and Buildings* **158** 964-970.

[14] Y. NASSAR, ET AL. (2023) Thermal analysis of air-heating flat-plate thermal solar collectors. *International Journal of Electrical Engineering and Sustainability* **1** 129-144.

[15] M.H. MACHI, I. FARKAS, J. BUZAS (2024) Enhancing solar air collector performance through optimized entrance flue design: A comparative study. *International Journal of Thermofluids* **21** 100561.

[16] H.K. VERSTEEG (2007) "*An introduction to computational fluid dynamics the finite volume method, 2/E*". Pearson Education, India.

[17] S. PATANKAR (2018) "*Numerical heat transfer and fluid flow*". CRC press.

[18] F.P. INCROPERA, ET AL. (1996) "*Fundamentals of heat and mass transfer*", Vol. 6. Wiley, New York.

[19] F. MOKHTARI, D. SEMMAR (2001) L'Influence de la Configuration de l'Absorbeur sur les Performances Thermiques d'un Capteur Solaire à Air. *Revue des Energies Renouvelables: Days Thermal*, pp. 159-162.